Contents lists available at ScienceDirect

Ocean Engineering

journal homepage: www.elsevier.com/locate/oceaneng

Highlights

Unsteady hydrodynamic loads on energy saving ducts

Ocean Engineering xxx (xxxxx) xxx

P. Anschau, N. Kornev*, S. Samarbakhsh

- Unique measurements of unsteady pressures on energy saving duct (ESD).
- Unique measurements of unsteady forces on ESD.
- High-fidelity CFD with resources acceptable for industrial applications.
- Detection of significant unsteady loads on ESD.

Contents lists available at ScienceDirect

Ocean Engineering

journal homepage: www.elsevier.com/locate/oceaneng

Unsteady hydrodynamic loads on energy saving ducts

P. Anschau [a], N. Kornev [b,*], S. Samarbakhsh [b]

[a] Potsdam Model Basin, Marquardter Chaussee 100, 14469 Potsdam, Germany
[b] Chair of Modeling and Simulation, University of Rostock, 18057 Rostock, Germany

ARTICLE INFO

Keywords:
ESD
Bulker
URANS
LES
Hybrid methods
Experimental Fluid Dynamics

ABSTRACT

Energy-saving ducts (ESD) attract much attention because of their significant ability to increase ship efficiency. Along with the issues of hydrodynamic interaction with the propeller and the hull, hydrodynamic loads on ESD and especially unsteady loads are of interest for ESD strength assessment. The paper presents complex experimental and numerical investigations performed to study unsteady pressures and forces acting on ESD due to wake nonuniformity and turbulence. The computations were performed using a hybrid URANS/LES approach. Force and pressure measurements with a high temporal resolution were carried out in the Potsdam ship model basin. Both numerical and experimental studies revealed strong unsteady pressure fluctuations and high oscillating forces on the duct which are increased by the propeller suction. The root mean squares of the fluctuation of axial, transverse and vertical forces are, respectively, 1.5, 0.8 and 0.4 percent of the total propeller thrust. The results can be useful for the prognosis of structural problems for energy saving ducts.

1. Introduction

Reduction of fuel consumption and emission required by the Energy Efficiency Design Index (EEDI), which was introduced by the International Maritime Organization, is a very urgent problem in shipbuilding. One of the promising ways to solve this problem is the development of Energy-Saving-Devices (ESD), which are capable increasing ship propulsion efficiency by 3%–10%. ESDs can be subdivided into the three following groups:

• ESD in front of the propeller, which improve the inflow to the propeller by wake equalizing (ducts) or by creating a favorable swirl in front of the propeller using fins as a pre-swirl stator (PSS). There are pre-swirl ducts, for instance the Mewis ducts, which combine both effects, i.e. wake equalizing and swirl. Properly designed ducts and PSS are able to generate thrust which results in a further increase of the ESD efficiency.

• ESD behind the propeller, which regain the energy losses due to circumferential speeds. These include, for example, thrust fins and propeller boss cap fins.

• Combination of ESD behind and in front of propellers.

Efficiency of various propulsion-improving measures is compared, for instance, in Mewis and Hollenbach (2006). The present paper focuses on unsteady hydrodynamic effects on energy saving ducts of the Mewis type. Therefore, only duct related publications are mentioned below.

Most of published works concentrate on power gain and interaction with the hull caused by ducts. Hollenbach and Reinholz (2011) examined various ESD experimentally, such as ducts, PSS, thrust fins, stator fins and documented a delivered power reduction ranging from three to six percent. The energy transformation in the hull- ESD- propeller system is analyzed in the work of Terwisga (2013) with the help of an actuator disc model of the propeller and it was found that the efficiency of the duct depends on the thrust loading coefficient. CFD study of wake equalizing ducts presented in Korkut (2006) and Celik (2007) revealed up to ten percent power gain.

The swirl generating ducts (pre-swirl duct) are the focus of the work of Shin et al. (2013). An optimal form of eccentric duct was designed using CFD calculations and propulsion tests. Circular and non-circular ducts were studied, including a semicircular duct. With the latter, about five percent reduction in power requirement was achieved. A study of the scale effect on a concentric circular duct was carried out in the work of Sakamoto et al. (2014) who utilized a CFD method with overlapping grids. It has been proven that ESD must be studied to account for scale effects because of different influences of ESDs on the propeller suction. For a full (i.e. high block coefficient) ship model, the propeller suction effect decreases through the ESD application whereas it increases for large scale ships. For more slender hulls with smaller block coefficient the trend is opposite. A combination of semi-duct and pre-swirl stator, proposed in Schuiling (2013) and called the BSD, allows one to reduce the power by almost four percent. The increase of

* Corresponding author.
E-mail address: nikolai.kornev@uni-rostock.de (N. Kornev).

https://doi.org/10.1016/j.oceaneng.2022.113431
Received 21 September 2022; Received in revised form 25 November 2022; Accepted 11 December 2022

the hull resistance due to ESD is about two percent which is close to the results of the measurement and calculations performed in this paper. CFD was used in Kim et al. (2015) to develop a new ESD based on the combination of a duct and a pre-swirl stator (PSS) which is installed inside the duct. Optimal profiles for both the duct and PSS have been designed to achieve approximately six percent reduction in delivered power P_D. The measurements in the towing tank have fully confirmed these results. This design is very similar to the Mewis duct (Guiard et al., 2013), which includes the three following elements: non circular duct with the axis above the propeller axis, PSS inside the duct, and propeller with increased loads on the inner radii and improved cavitation characteristics at blade tips. An overview of CFD simulations for Mewis ducts can be found in Guiard et al. (2013) and Mewis and Guiard (2011). According to the experience of Becker Marine Systems the power gain of a Mewis duct ranges from three to five percent for multipurpose vessels, from five to seven percent for tankers and from six to eight percent for bulk carriers (https://www.becker-marine-systems.com/products/product-detail/becker-mewis-duct.html).

The ship model JBC (Japan Bulk Carrier) equipped with ESD in the form of an axially symmetric duct was one of the test cases at the Tokyo 2015 Workshop on CFD in Ship Hydrodynamics. It was clearly shown that the RANS (Reynolds Averaged Navier Stokes) calculations for drag agree very well with measurements with an error less than five percent. All RANS models predict a reduction in power due to the ESD application but this is much lower than the measured results. In the majority of the calculations an increase of the thrust deduction fraction is documented, while in the measurement and in Yin et al. (2015) the suction effect becomes smaller when ESD is installed. This effect also correlates with results of Sakamoto et al. (2014). Although the simulations of Yin et al. (2015) were obtained with a relatively low number of cells (about 5 Mio) using overlapping grids and no grid convergence study was performed, the power gain and the suction effect were predicted with good accuracy. Ship drag decrease due to ESD is registered in measurements as well as in all CFD calculations except (Schuiling et al., 2015) who made an important comment on ESD modeling. The authors note that the drag increase due to ESD in CFD calculations in real scale is more logical than the drag decrease, because the flow in CFD is assumed to be fully turbulent everywhere, while part of the duct flow remains laminar in measurements due to low local Reynolds numbers. Accordingly, the resistance of the duct is somewhat lower in measurements than in CFD calculations in real scale. As a result, power gain in CFD calculations in real scale is lower than in model scale measurements. In principle, we agree that the flow on a part of the duct and especially on fins can be laminar and the friction drag is underestimated. However, the pressure drag can be overestimated in measurements due to flow separation on fins which is quite probable in laminar and low Reynolds number flows. Both these effects can cancel each other. Therefore, the scale effect problem needs further thorough investigations in the future. A recent review of state of the art on ESD can be found in Lee et al. (2021).

Knowledge of unsteady loads on ducts are necessary for the structural design of ESD and their attachment to the hull. The propeller and ESD are located in the wake of the hull, which is non-uniform and turbulent. Unsteady loads on the duct and propeller are caused by:

- Inhomogeneity of the averaged nominal wake;
- Turbulence of the nominal wake; and
- Unsteady ship motion, e.g. during motion in waves and/or maneuvering.

The first and the last effects are numerically studied in the paper of Bakica et al. (2020) which is focused on the mean pressure distribution and loads on the duct both at calm water conditions and in waves. CFD simulations demonstrated a big influence of the propeller suction on the pressure distribution. It was also shown that the ship with a duct possesses a higher thrust loss in waves than without a duct. Experimental results on the surface pressure distribution on a duct in calm water and in waves are presented in Kume and Fukasawa (2018). This work presents time history of pressure signals obtained from pressure transducers whose design suggests that only low frequencies are captured. The forces on the duct are not presented. High frequency pressure fluctuations and forces on the duct have still not been measured.

Based on the literature review, one can conclude that for the calculation of ship hull with ESD and propeller, only (U)RANS methods have been used and unsteady loads due to non-homogeneity and turbulence in the wake have not been investigated so far. These unsteady loads, which are mainly relevant for ships with a large degree of fullness, are the focus of the present project. In our previous works (see e.g. Kornev and Abbas (2018)) it was shown that if the mean wake field is satisfactorily modeled with modern URANS (Unsteady Reynolds Averaged Navier Stokes) methods, the instationarity is completely lost. These physical effects can only be captured by the so-called scale-resolving techniques (SRS) which include Large Eddy Simulation (LES), Scale Adaptive Simulation (SAS) and various variants of hybrid URANS/LES methods. The latter approach is utilized in this paper. The scale resolving DES simulation were already utilized for the numerical study of an idealized configuration of a duct with propeller without a ship hull in Lungu (2021). In this work we present results for the whole ship model including hull, duct with four fins, propeller and rudder.

2. Mathematical model

The mathematical model includes the continuity equation for the incompressible flow

$$\frac{\partial \overline{u}_i}{\partial x_i} = 0 \tag{1}$$

and the momentum equation

$$\frac{\partial \overline{u}_i}{\partial t} + \frac{\partial(\overline{u}_i \overline{u}_j)}{\partial x_j} = -\frac{\partial \overline{p}^*}{\partial x_i} + \frac{\partial(\tau^l_{ij} + \tau^t_{ij})}{\partial x_j}, \tag{2}$$

written both for the velocity $\overline{u}_j$ and pressure $\overline{p}$. In RANS zones the overline means the Reynolds average whereas in LES it means the spatial filtering. Here we use the standard notation of p^* for the pseudo-pressure and τ^l_{ij} and τ^t_{ij} for the laminar and turbulent stresses, respectively. The three following turbulent models were utilized for calculation of τ^t_{ij}: (1) RANS Model (k-ω SST) by Menter (1994). (2) Hybrid IDDES (Improved Delayed Detached Eddy Simulation) model by Shur et al. (2008). The IDDES routine available in OpenFOAM is based on the Spalart Allmaras (SA) and k-ω SST URANS turbulence models (3) Hybrid Model LH and SLH models developed in our works Kornev et al. (2011), Abbas et al. (2015) and Shevchuk and Kornev (2018).

The computational domain in our model is dynamically (i.e. at each time step) subdivided into the LES and URANS regions. The key quantities of this decomposition are a certain length scale $\tilde{L}$ and the extended LES filter Δ, which are computed for each cell of the mesh. A cell of the mesh belongs to one area or the other, depending on the value of $\tilde{L}$ relative to Δ: if $\tilde{L} > \Delta$ then the cell is in the LES area, otherwise it is in the URANS region.

The filter Δ is determined as $\Delta = \sqrt{0.5(d^2_{\max} + \delta^2)}$, where $d_{\max}$ is the maximal length of the cell edges $d_{\max} = \max(\Delta_x, \Delta_y, \Delta_z)$ and $\delta = \sqrt[3]{(\text{the cell volume})}$ is the common filter width used in LES. $\tilde{L}$ is expressed through the integral length L multiplied with a shielding function f_d

$$\tilde{L} = L f_d, \tag{3}$$

The length L is determined from the formula of Kolmogorov and Prandtl, which is valid for high local Reynolds numbers in the wake area and on the outer boundary of the boundary layer:

$$L = k^{3/2}/\varepsilon = \frac{\sqrt{k}}{0.09\omega} \tag{4}$$

where k is the turbulence kinetic energy, ε is the dissipation rate and ω is the specific dissipation rate. The introduction of shielding in Shevchuk and Kornev (2018) was necessary to force the RANS/LES interface to move farther from the wall and to reduce the grid induced separation in a way which is analogous to transformation of DES to DDES. The shielding function reads:

$$f_d \equiv 1 - \tanh([8r_d]^3), \text{ with } r_d \equiv \frac{\nu_t + \nu}{\kappa^2 y^2 \sqrt{0.5(S^2 + \Omega^2)}}. \quad (5)$$

In the boundary layer the function f_d tends to zero and reduces the integral length scale to zero near the wall, so that the ratio $\tilde{L}/\Delta$ is kept small in the vicinity of the body. The model therefore switches to RANS near the wall, regardless of the mesh resolution. The extended LES filter Δ depends only on the geometry of the mesh and is computed only once, whereas the length scale $\tilde{L}$ is changed in space and varies from one time step to another, which results in dynamic decomposition of the computational domain into the LES and URANS regions. The model with $f_d = 1$ is further referred to as the LeMoS hybrid, otherwise it is Shielded Lemos Hybrid SLH.

The turbulent stress τ^t_{ij} is calculated from the Boussinesq approximation using the concept of the turbulent viscosity which is considered as the subgrid viscosity in the LES region. These stresses are computed according to the localized dynamic model of Smagorinsky in the LES region and according to the $k-\omega$ SST turbulence model of Menter (1994) in the URANS region. The turbulent kinematic viscosity is smoothed between the LES and URANS regions using the empiric blending function:

$$\nu(x) = \alpha \nu_t + (1-\alpha)\nu_{SGS} \quad (6)$$

$$\alpha(x) = \frac{1}{\pi} \arctan\left(\frac{-40x}{x_2 - x_1} + 10\frac{x_2 + x_1}{x_2 - x_1}\right) + \frac{1}{2} \quad (7)$$

where ν_t is the RANS turbulent kinematic viscosity, ν_{SGS} is the LES subgrid viscosity, $x = (L/\Delta - x_1)/(x_2 - x_1)$ and $x_1 = 0.95$ and $x_2 = 1.05$ are two empiric constants. The factor 40 in the arc tangent function is chosen such that $\nu \approx \nu_{SGS}$ when $L/\Delta > 1.05$ (LES region) and $\nu \approx \nu_t$ when $L/\Delta < 0.95$ (RANS region) and for $0.95 < L/\Delta < 1.05$. This expression gives a smooth transition of ν between the two regions. The wall functions can be used in the near wall URANS region. The hybrid model was thoroughly validated in Abbas et al. (2015) and Abbas and Kornev (2016a,b).

3. Numerical implementation

The CFD calculations using both URANS and hybrid models were carried out with solvers from open source CFD software, OpenFOAM (Jasak, 1996; Weller et al., 1998). The spatial discretization of the convective term in the momentum equation is performed using the limitedLinear scheme implemented in OpenFOAM which tends towards an upwind scheme in regions of rapidly changing gradient. This scheme uses a coefficient ranging from zero to one. For the current work the coefficient is set to 0.25 after some initial time steps. The Laplacian term was discretized with the Gauss theorem and linear interpolation with non-orthogonal correction. The pressure gradient was reconstructed using a linear scheme based on the Green–Gauss theorem. The auxiliary equations of k and ω were discretized in the same manner except for the convective term, for which a van Leer's total variation diminishing (TVD) scheme was used. The time discretization has been done using the second-order Crank–Nicolson scheme. For the initialization of the flow in the computational domain the steady RANS solutions were used.

The size of the computational domain was chosen as follows. In order to minimize the boundary influence the computational domain is extended to $2L_{pp}$ in front of the ship, $4L_{pp}$ in the downstream direction, $3L_{pp}$ towards the starboard and portside and $2L_{pp}$ towards the bottom. The symmetry plane was located at $z = 0$. The model scaled ship hull is 1/30 of the full designed model. Computational grids are generated with cfMesh (Juretić, 2022) tool integrated within OpenFOAM. cfMesh provides hexahedral-dominated unstructured mesh.

The computations for the bare hull have been carried out with the fixed maximal Courant number Co of 0.6 for all grids. The unsteady solver pisoFoam was used for these calculations. The bare hull was studied with three gradually refined grids generated by cfMesh and containing 10M, 19M and 33M cells. A strong refinement was performed in the propeller disc. All grids were obtained from the 10M grid by gradual refinement. The wall functions, based on Spalding velocity profile, were applied.

The unsteady moving solver pimpleFOAM was used for the calculations of the ship with rotating propeller. Computations for the system of the ship with rotating propeller have been carried out with the fixed maximal Courant number of 85 for $n = 9.45$ rps, which corresponds to the time step 5×10^{-4} s. The number of internal iterations was fixed at 20, which was proven to be high enough to reach the convergence. For $n = 9.45$ rps of the propeller, the increment for the rotation angle of the propeller for each time step is equal to 1.71 deg. The rotating propeller was calculated using the Arbitrary Mesh Interface (AMI) provided in OpenFOAM to model the interface between static (hull) and rotating (propeller) grids. The ship with rotating propeller was studied with 19M grid cell for hull and duct plus 3M cells for propeller. The static grids have been generated using the cfMesh and the grid for rotating propeller is generated with Pointwise (see Section 5.2). In simulations, the non dimensional residual for the pressure, velocity, kinetic energy and vorticity are varied in ranges of $5 \cdot 10^{-3}$, $10^{-7} - 10^{-8}$, 10^{-7} and $10^{-8} - 10^{-9}$, respectively.

4. Experimental setup

The measurements of the model resistance, forces on the duct and the surface pressure distribution were performed in the towing tank of SVA Potsdam. The towing tank is 280 m long and has a rectangular cross-section of 9 m width and 4.5 m depth. The towing carriage is driven via two double stator linear motors and can achieve a speed up to 7.5 m/s with an accuracy of 0.6 mm/s (see for details https://www.sva-potsdam.de). The ship investigated in this paper is the $M1749S030$ bulk carrier whose ship lines are very close to those of the well known benchmark test case JBC. The particulars of the model and its propeller are presented in Tables 1 and 2. The sketch of the duct geometry is illustrated in Fig. 1.

The surface pressure distribution was measured at eight probes shown in Fig. 6 using sensors of type MS58XX that were configured to measure pressure fluctuations at a sampling rate of 200 Hz with a resolution of 0.11 Pa. The diameter of the pressure transducers determining the spatial resolution is 3 mm. To measure the forces acting on the duct, the model was manufactured in a way that separated the duct from the hull (see Fig. 2). The duct was mounted on a 6-component dynamometer installed into the hull, sampling the six components of forces and moments with a sensitivity of 2 mV/V at a frequency rate of 2.4 KHz.

The measurements with rotating propeller were performed in design (n = 9.45 1/s) and ballast (n = 7.97 1 /s) conditions. The draft on the stern and model speed are the same in both design and ballast conditions whereas the draft on the bow is less (tail-heavy ship) in ballast conditions. Correspondingly, the model displacement is smaller in ballast conditions.

A random measurement error ε of a quantity q can be estimated from analysis of scattering the measurement data in N = 20 measurements series. The experimental standard deviation of N pressure measurements is calculated as:

$$\varepsilon = \left(\sum_{i=1}^{N} \frac{1}{N}(\overline{q}_i - \langle q \rangle)^2\right)^{1/2} / |\langle q \rangle|,$$

Table 1
$M1749S030$ model hull particulars.

L_{PP}, m	B_{WL}, m	T, m	A_W, m^2	∇, m^3	C_B	Scale parameter λ	V m/s	Re	Fn
6.0	1.0	0.35	5.5933	1.7093	0.794	30	1.32	$7.4 \cdot 10^6$	0.169

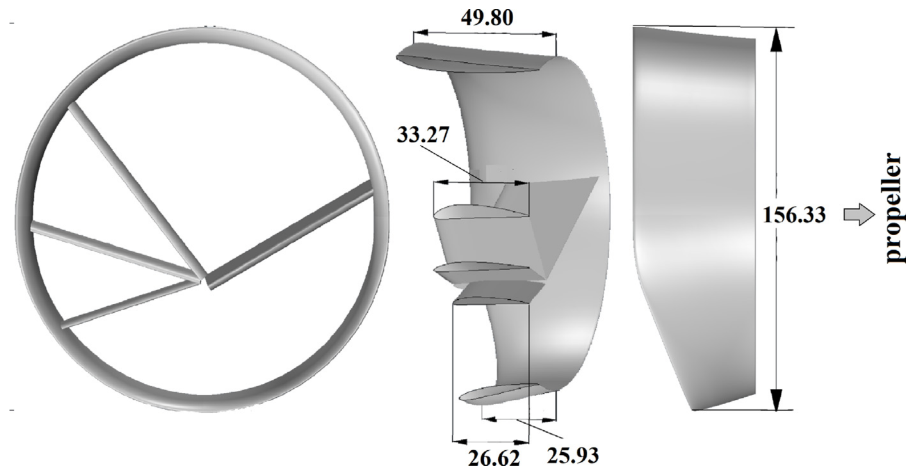

Fig. 1. Sketch of the geometry of the duct before installation on the hull (see Fig. 6). The sizes are given in mm.

Table 2
Propeller model particulars.

Propeller	Rotation	Z	D, m	$P_{0.75}/D$	$c_{0.75}$, m	A_E/A_0	n, rps
$P1920$	Right handed	4	0.21	0.76	0.044	0.4	7.97 and 9.45

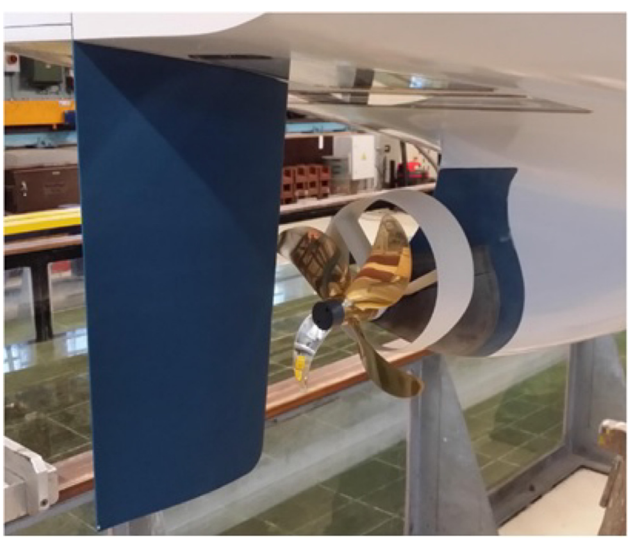

Fig. 2. Stern area of the $M1749S030$ ship model equipped with the Mewis duct, rudder (blue) and propeller. (For interpretation of the references to color in this figure legend, the reader is referred to the web version of this article.)

where $\overline{q}_i$ is the averaged value in ith measurement and $\langle q\rangle = \frac{1}{N}\sum_{i=1}^{N}\overline{q}_i$. This random error ε, averaged over eight sensors, is around 2.5 percent for both the averaged pressure and its pulsations presented in Tables 4 and 5. This error is dominating because the error of the absolute pressure sensors is only 0.125 percent. The standard uncertainty of repeat tests can be obtained from ε dividing it by $\sqrt{N}$ (see ITTC (2014)). The random error for the averaged forces on the duct $\overline{F}_x$, $\overline{F}_y$ and $\overline{F}_z$ are, respectively, three, eight and twelve percent whereas for the fluctuations F_x', F_y' and F_z' the error does not exceed three percent. The error of the force sensor is 0.2%.

5. Results

5.1. Bare hull drag

Although the aim of the paper is the study of unsteady effects we start the description of numerical results with an analysis of the bare hull drag to evaluate the credibility of the hybrid simulations. The results of the drag computations are given in Table 3. The RANS $k-\omega$ SST model (column 2), which is well adapted for computations of well streamlined bodies, agrees well with measurements of the SVA Potsdam (Experimental Fluid Dynamics, EFD, column 1). OpenFoam calculations with the hybrid IDDES SST model (column 3) are very close to those of the RANS $k-\omega$ SST. Clarification of such a good agreement with both EFD and RANS data revealed that the IDDES SST model implemented in OpenFoam does not activate the LES branch and remains a pure RANS model at least for the grid resolution used in these computations. This was clearly demonstrated by the analysis of the velocity field in the wake which was proven to be time independent in IDDES simulations. On the contrary, the IDDES SST simulations performed in STAR CCM+ with the same mesh (column 4) demonstrated strong unsteadiness in the wake and a clear activation of LES branch at some distance from the body. A possible reason for such a different behavior of the same model in two different codes is a disadvantageous implementation of the hybrid model in OpenFoam caused most likely by different calculation of filtering. Any deep investigation of this shortcoming, observed also by other authors Mockett et al. (2015) and Taranov (2021), was not undertaken in the present work because the hybrid models proposed by the authors LH (column 5) as well as SLH (columns 6 and 7) reproduced unsteady effects properly.

The accuracy of hybrid calculations with the activated LES branch (columns 4, 5 and 6) is lower than that of URANS computations (columns 2 and 3). This is in accordance with the experience gathered in application of hybrid simulations to ship hydromechanics problems. These experiences show that the indisputable advantage of hybrid approaches is their ability to reproduce unsteady flow effects. However, the accuracy of the solution of more simple tasks like determination of the resistance is sometimes proved to be lower than that of RANS approaches. This accuracy reduction is due to the underestimation of the friction resistance and overestimation of the pressure one. For instance, our simulations (Kornev et al., 2019) show that the total

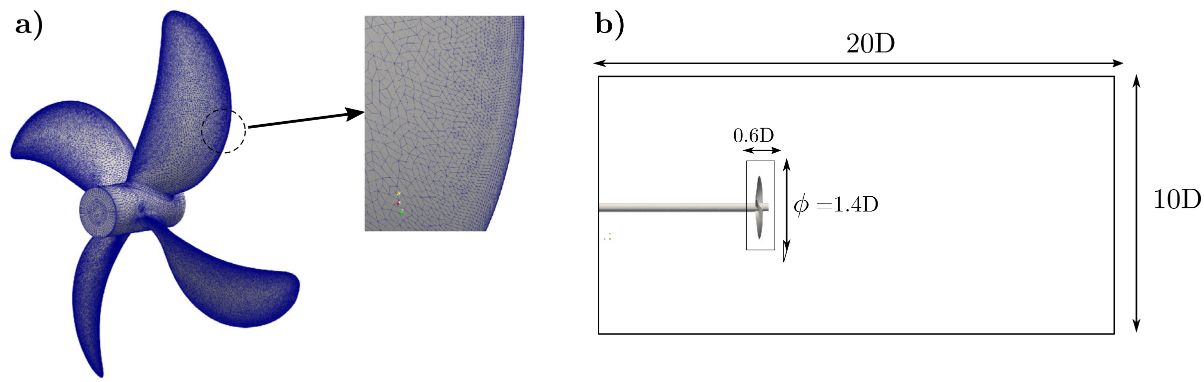

Fig. 3. (a). Propeller surface mesh, isotropic triangles in the core of the mesh with stretched right-angled triangles layers towards the leading edge. (b). The size of the computational domain for propeller open water test.

Table 3
The total drag coefficient C_t of the bare hull $M1749S030$. OF stands for OpenFOAM, EFD for Experimental Fluid Dynamics.

	1	2	3	4	5	6	7
Method	EFD	$k-\omega$ SST	IDDES SST	IDDES SST	LH	SLH	SLH
Code Generator		OF cfMesh	OF cfMesh	STARCCM+ cfMesh	OF cfMesh	OF cfMesh	OF Pointwise
Grid Averaged y^+		33M 19	33M 21	33M 21	33M 19	33M 19	29M 18
$C_t \cdot 10^{-3}$	3.92	4.08	3.96	3.6	3.12	3.36	3.91

resistance C_t is determined with a high accuracy whereas the friction component C_f was sufficiently underestimated whereas the pressure one C_p was overestimated. This fact was explained as being caused by an ambiguous grid which is finer than the RANS grid but is still too coarse for proper LES simulations. As a result, the LES solution penetrates closer towards the wall and, being under resolved, caused reduced turbulent friction. Additionally, the coarse grid resolution causes the grid induced separation which results in the overestimated pressure drag. This disadvantage of hybrid simulations was documented in all our calculations regardless of whether LH, SLH or (I)DDES models were used. This conclusion is also valid for STAR CCM+ IDDES computations. The best agreement with measurements for the total drag was achieved with the SLH model for the Pointwise grid (column 7). Application of Pointwise allowed introduction of thirty prism layers in the boundary layer whereas only from eight to ten layers was possible using cfMesh. As a result the flow in the boundary layer becomes much smoother and the accuracy of drag prediction is substantially improved.

5.2. Propeller at open water conditions

Since the ship model is calculated with a rotating propeller, an additional validation study was performed for the propeller at open water conditions. A high quality unstructured mesh was created using Pointwise which generates a combination of anisotropic and isotropic surface meshes. The area of high curvatures such as the propeller leading and trailing edges are treated carefully using layers of stretched, right-angled triangles to accurately resolve the geometry curvatures, Fig. 3-a. The surface mesh away from the blade edges was covered by isotropic triangles generated by Delaunay algorithm in Pointwise. The computational domain includes a far-field rectangular box and an MRF cylindrical domain around the propeller. The size of the cylindrical MRF and farfield box is presented in Fig. 3-b. The dimensions are based on the propeller diameter. The volume mesh is a combination of the tetrahedral cells and high quality prism layer grid on the propeller surface. The total mesh cells is about 6Mio including 3.8Mio in the MRF region and 2.1Mio in the far-field rectangular box. The RANS simulation has been done with kω-SST turbulence model. The propeller rotational speed is considered constant with the value of 7.9 [1/s]. The inlet velocity varies from 0.248 [m/s] to 1.327 [m/s] and the obtained advance coefficient based on the inlet velocity is between J = 0.15 and J = 0.8. In the post-processing step propeller quantities such as efficiency, thrust coefficient and torque coefficient have been evaluated. The results presented in Fig. 4 illustrate very good agreement with the measurements of SVA Potsdam. The rotating grid around the propeller was then used for calculations of the whole ship model arrangement including the duct, propeller and rudder.

5.3. Turbulent pressure fluctuations on the duct

Steady pressure distribution on the ESD duct has already been studied in experimental (Kume and Fukasawa, 2018) and CFD (Bakica et al., 2020) works. The unsteady effects studied in Bakica et al. (2020) were caused by the ship oscillations. In this section we present unsteady pressure fluctuations caused by the turbulent wake flow. In this case, strong unsteady pressure fluctuations and loadings on the duct arise due to the flow structures forming in the stern area of the hull (see Fig. 5). As experience shows, not only the unsteady fluctuations caused by these structures but also the mean wake prediction require the application of hybrid methods.

5.3.1. The case without propeller

The results for the case without propeller determined from computations and measurements by SVA Potsdam are presented in Fig. 7 at some selected probes displayed in Fig. 6. As seen, the URANS $k-\omega$ SST calculations (Fig. 7) do not resolve the unsteady high frequency fluctuations of the pressure. Only small low frequency regular oscillations are documented. In contrast, the hybrid simulation brings substantial irregular fluctuations of the pressure which are more physical as the measurements show.

There is a slight contradiction with respect to the mean pressure level in measurements and calculations (see Table 4) which can be caused by the wave surface deformation. In CFD calculations the single phase flow model was applied with simulation of the free surface by a symmetry boundary condition. The hydrostatic part of the pressure was not added to the total pressure. In the measurements the hydrostatic part ρgh was subtracted from the total pressure and h was taken as the submergence of the sensor under the unperturbed free surface. Although the Froude number 0.169 is low, small waves appear in the bow and stern areas of the hull. If the wave height over the sensor is only, say 5 mm, it makes 50 Pa difference in the mean pressure level. The maximum deviation between the mean pressure in CFD hybrid simulations and measurements at P1 lies in this range. Higher deviations between URANS and measurements at point 2 can be explained

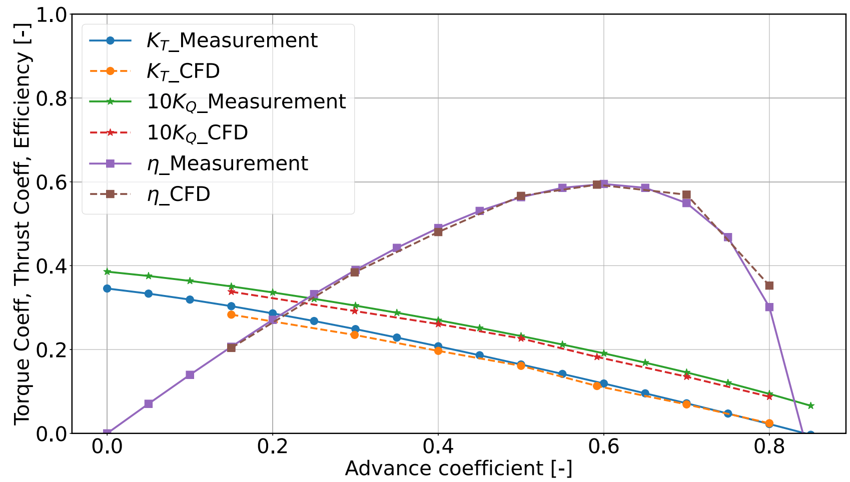

Fig. 4. Open-water diagram of the $M1749S030$ propeller calculated using $k-\omega$ SST model. The error of SVA measurements is estimated around 0.21% for both the torque and the thrust.

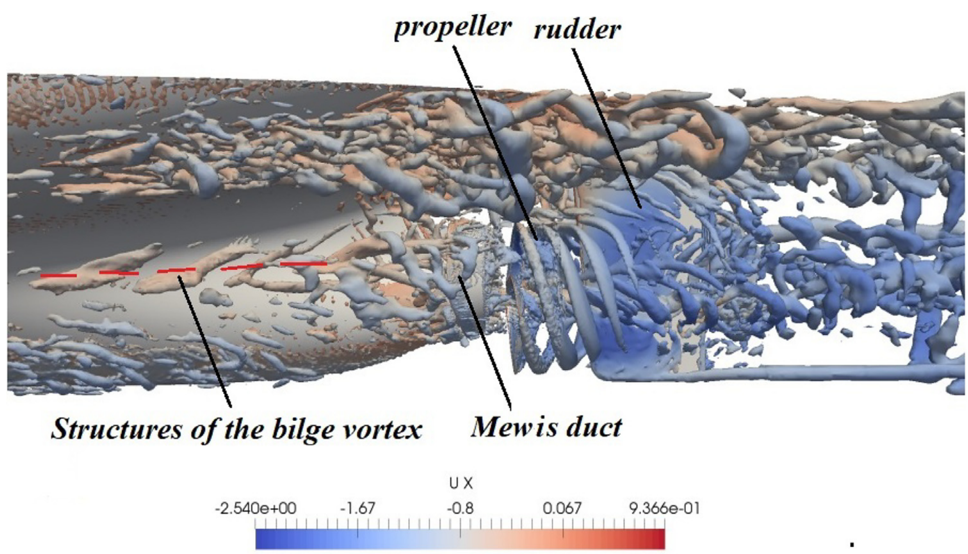

Fig. 5. Visualization of vortex structures in the stern area of $M1749S030$ using $Q = 100$ criterion. Results achieved with SLH computations.

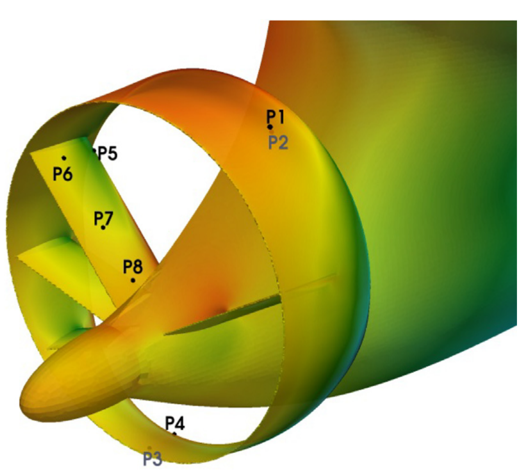

Fig. 6. Pressure probes on the duct used in measurements and calculations. The probe P2 is beneath the probe 1 on the inner side of the duct. The probe P3 is located on the outer side of the duct.

Table 4
Results of pressure computations at different probes without propeller.

Probe number	Mean $\overline{p}$ Pa		Pulsation $\overline{(p-\overline{p})^2}^{1/2}$ Pa		Dominating frequency Hz	
	CFD	EFD	CFD	EFD	CFD	EFD
1	193	147	19.2	18.8	2.22	2.24
2	74	90	26.5	20.5	2.22	2.24
3	112	84	32.2	23.5	1.97	1.52
4	169	121	41	31.7	1.97	1.72
5	77	82	75.5	32.6	2.46	2.74
6	122	112	15.9	19.3	2.46	2.20
7	129	101	14.4	14	2.28	2.24
8	153	140	15.3	14.8	1.73	2.24

by less accurate prediction of the mean flow in the wake region, as it was convincingly shown for the JBC benchmark test (see, for instance, Figure 5 in Kornev et al. (2019)).

Qualitatively, the change of the fluctuations $\overline{(p-\overline{p})^2}$ depending on the probe position is the same in CFD and EFD (Table 4). Quantitatively, there is a substantial deviation at points 3 and 4 and it is especially large at P5. These points are located close to the leading

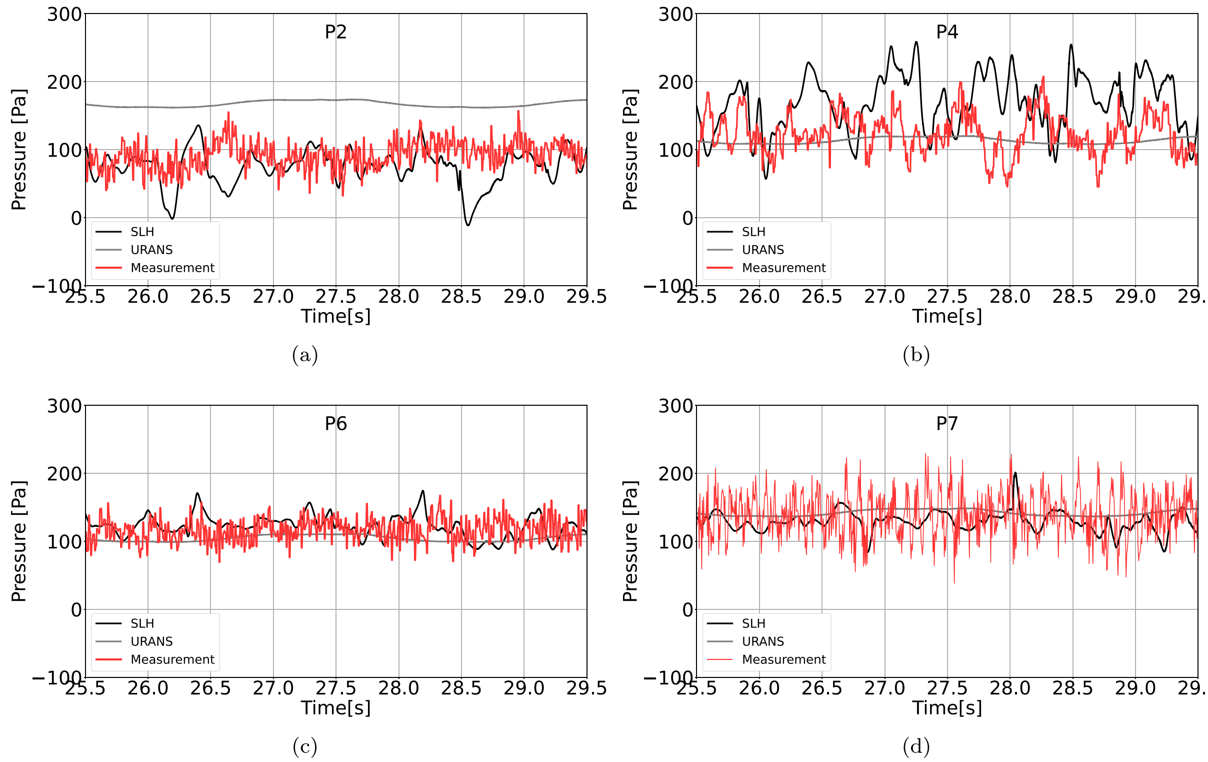

Fig. 7. Time history of pressure fluctuations on the duct without propeller obtained from $k-\omega$ SST and hybrid SLH calculations.

edge, at which a strong interaction between the profile and incoming vortex structures, which cause a large temporal variation of the local angle of attack, is expected. The point 5 is located in the corner at the junction of the duct surface and fin. Here one can expect the formation of the conjunction vortex and an increased interaction of both leading edges with incoming vortices. An additional reason for the increase of fluctuations and deviation between CFD and EFD at points 3 and 4 is that these points are closest to the hull (see Fig. 6) in the area of strong boundary layer influence. Obviously, an accurate computation of the flow near these points requires a more fine computational grid to achieve a better agreement between CFD and EFD.

Spectra of pulsations determined experimentally is difficult to analyze because they contain many peaks of non hydrodynamic nature (mechanical, electrical, etc.) which are hard to distinguish from the hydrodynamically caused ones. On the contrary, the peaks gained from CFD can easily be interpreted solely from the hydrodynamic point of view. It was found, that all CFD and EFD spectra have a well pronounced peak at a low frequency documented in Table 4 for all probes. We suppose, that the low frequency dominating mode is caused by big vortex structures shed from the hull in the stern area (see Fig. 5).

In our previous study (see Albertzard (2022)) the integral length L of the flow, obtained from a hybrid simulation, is estimated as $\sim$23 mm in front of the duct. The length is calculated from the definition $L = \int_0^{\infty} \rho_{11} dx$ where ρ_{11} is the autocorrelation function of the longitudinal velocity fluctuation u'_x. The length of the vortex structure $L_v = \int_{-\infty}^{\infty} \rho_{11} dx$ is twice as large as L, i.e. $L_v \sim 46$ mm. The velocity in front of the duct $\bar{u}_x$ is varied between 0.1 and 0.4 m/s (Fig. 8). The vortex structures cause the pressure change on the duct surface due to three reasons. First, they have a reduced pressure inside of them and cause the pressure oscillations when flowing through probe points even without a hydrodynamic interaction with the duct. Second, they cause the reduction of the incident longitudinal velocity on the duct. Third, they increase or decrease the angle of attack on the duct depending on their rotation. The two latter mechanisms cause the change of the pressure and force on the duct. The minimum period of pressure oscillation T_{min}, if the flow is tightly packed by structures, can be estimated as $T_{min} = L_v/\bar{u}_x$ which results in the maximum frequency range $\bar{u}_x/L_v$ from 2 to 8 Hz. Since the flow is not tightly packed by structures and there are gaps between them, and since the rotation direction of the structures alternates, this range is substantially shifted towards smaller frequencies.

This analysis should be considered with care because the definition of L is strictly valid only for homogeneous flows which is not the case for ship flow wakes. There are also difficulties with computation accuracy of L at moderate grid resolutions. However, this simple analysis explains the presence of low frequent oscillations and the predicted range of frequencies has a certain overlapping with the range recorded in CFD and EFD study (see Table 4).

5.3.2. *The case with propeller*

The case with propeller was studied experimentally in design and ballast conditions. The effect of the propeller leads to a substantial increase of the pressure fluctuations indicating an enhancement of the wake unsteadiness. On one hand the suction effect of the propeller reduces the wake, diminishes the separations and can mitigate the unsteadiness. On the other hand increase of the flow velocity due to the suction amplifies the strengths of the vortices forming in the stern area, which contributes to the velocity and pressure fluctuations. The second effect proved to be stronger than the first one. The presence of the propeller results in the appearance of regular pressure fluctuations in URANS simulations (Fig. 9) whereas the fluctuations gained from the hybrid simulations and EFD remain irregular and generally have a greater magnitude. With the propeller the hybrid simulations (Fig. 9) agree with measurements better than these of URANS with respect to the mean pressure value, amplitude of the pressure fluctuations and irregularity.

Like in the previous case without propeller, the pressure pulsations increase at points close to the leading edge of the duct (see Table 5). The maximum pulsation and maximum deviation between CFD and EFD take place at the probe P6 located in the junction between the duct and fin surfaces.

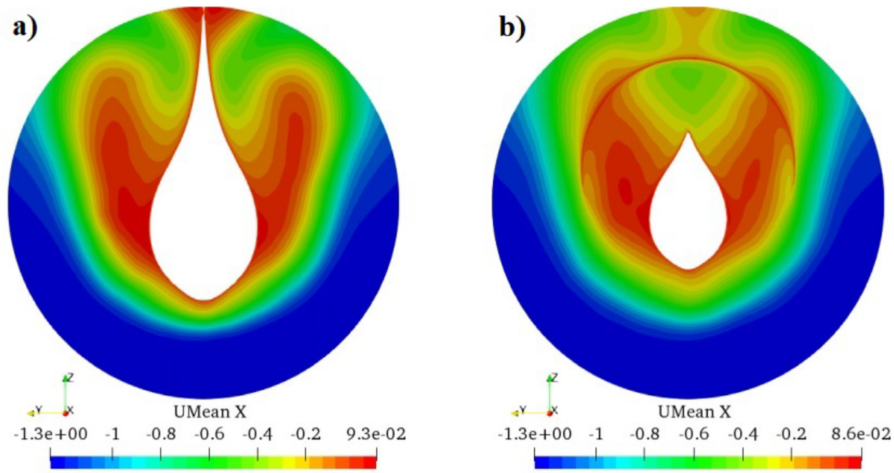

Fig. 8. Mean longitudinal velocity in front of (a) and at the leading edge of the duct (b). CFD SLH computations taken from Albertzard (2022). The red circle on the right picture displays the leading edge of the duct. (For interpretation of the references to color in this figure legend, the reader is referred to the web version of this article.)

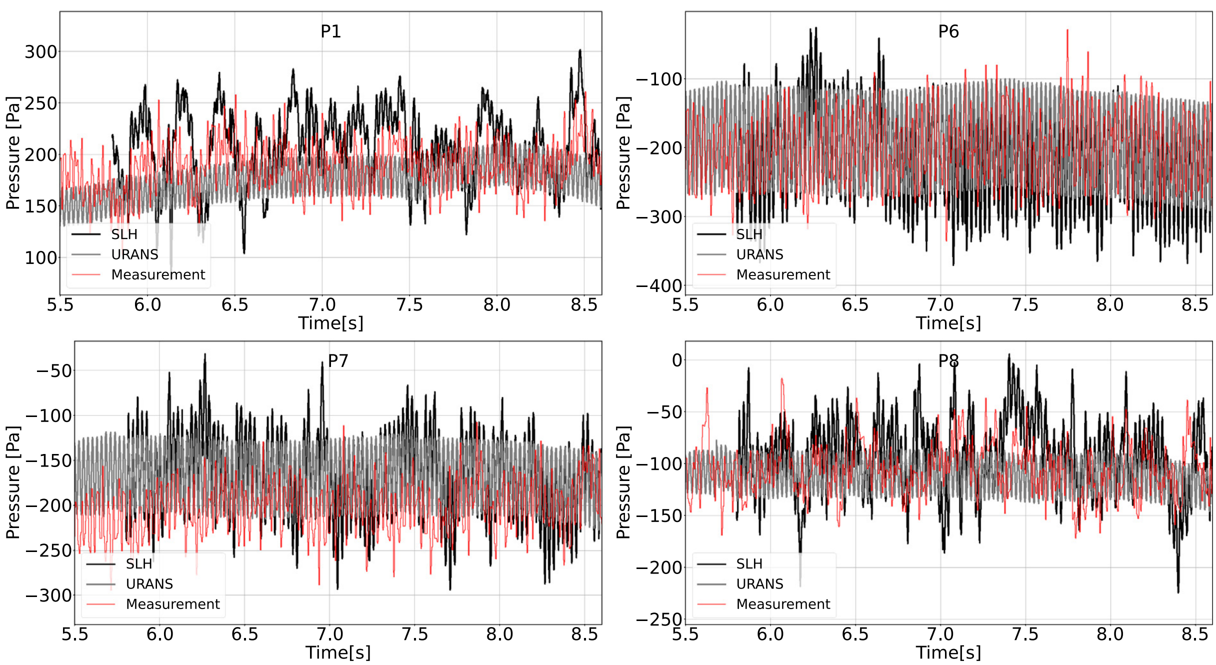

Fig. 9. Time history of pressure fluctuations on the duct with propeller.

The spectrum of pressure pulsations in the case with propeller does not reveal any new remarkable information. It shows peaks at blade passing frequencies (BPF) both in CFD and EFD. The magnitude of the BPF modes strongly decreases with the increase of the BPF number. The magnitude of the first BPF mode is a few orders higher than the second and third ones. The peak at low frequencies, observed in the previous case, was revealed again in EFD and CFD spectra. It is well pronounced in EFD at P1, P2, P3, P4 and P5 probes, whereas the peaks at P6, P7 and P8 are not identified. The dominating frequency in the low frequency range is around 2.10...2.40 Hz which agrees well with the estimation for the case without the propeller (Table 4). Obviously, the propeller induced increase of the velocity $\overline{u}_x$ in front of the duct is accompanied by an increase of the typical vortex size L_v so that the relation $\overline{u}_x/L_v$ remains nearly the same with and without propeller.

Bearing in mind that both spatial and temporal resolutions used for the calculations are very moderate, the agreement for unsteady pressure pulsations obtained above can be considered quite satisfactory.

Table 5
Results of pressure computations at different probes with propeller under design conditions. NI means that the pronounced maximum was not identified.

Probe number	Mean $\overline{p}$ Pa		Pulsation $\overline{(p-\overline{p})^2}^{1/2}$ Pa		Dominating frequency Hz	
P	CFD	EFD	CFD	EFD	CFD	EFD
1	235.54	190.2	35.93	34.2	3.33	2.36
2	−368.28	−506.2	60.77	54.4	2.33	2.24
3	−53.882	−98.9	46.32	43.9	NI	2.24 (weak peak)
4	−325.593	−700.6	80.12	53.6	6.5	2.20
5	−506.12	−962.8	133.21	113.9	3.5	2.12
6	−403.97	−360.8	144.48	76.2	6.0	NI
7	−278.40	−342.9	37.91	43.5	4.5	NI
8	−167.78	−208.2	30.60	35.4	2.33	NI

Table 6
Force fluctuations on the energy saving device in Newton.

Force component	Fluctuation $\sqrt{\overline{(F-\overline{F})^2}}$, Newton							
	Without propeller			Design			Ballast	
	EFD		CFD	EFD		CFD	EFD	
	Plast	Alum		Plast	Alum		Plast	Alum
F'_x	0.41	0.290	0.072	0.26	0.544	0.089	0.23	0.276
F'_y	0.40	0.178	0.33	0.63	0.291	0.40	0.73	0.168
F'_z	0.47	0.096	0.215	0.58	0.138	0.28	0.28	0.081

6. Unsteady forces on the duct

For the case without propeller a small axial force arises on the duct both in EFD (−0.11 N) and CFD (−0.15 N). Since the force is negative the duct generates the drag. On the contrary, the duct contributes to the thrust when the propeller is activated. The axial force becomes 1.0 N in design and 0.58 N in ballast conditions. CFD predicts also the positive contribution to the thrust of 0.69 N in design conditions. In both design and ballast cases the thrust contribution is about 2.8 percent of the propeller thrust which is 35.63 N in design and 21.67 N in ballast conditions.

The experimental data were obtained for the duct made of plastics (Plast) and aluminium (Alum). The plastics duct experienced an increased vibration which forced us to manufacture and study the aluminium one. According to EFD prediction, the fluctuation of all three force components is essential (see Table 6) in design and ballast conditions regardless of the duct material. For the design condition and aluminium duct the root mean square fluctuation of the axial force is 0.54 N which is 1.5 percent of the total propeller thrust. The transverse and the vertical force fluctuation are, respectively, 0.8 and 0.4 percent of the total propeller thrust. The same ratios of force fluctuations to the total propeller thrust are valid in the ballast conditions. Fluctuations of F_y and F_z forces are higher in the case of plastic duct due to its increased vibration. The CFD data are in between plastic and aluminium duct EFD results. Compared to the total thrust, the fluctuations seem to be insignificant. However multiplied with λ^3, where $\lambda = 30$ is the scale factor, the fluctuations are essential. For instance, the root mean square fluctuation $F'_y = 0.291$N corresponds to ≈ 0.8 ton. The force amplitude $F_y - \overline{F_y}$ can be two or three times larger than the mean fluctuation (see Fig. 10). The reduced time averaged and fluctuating forces in ballast conditions are due to the reduced displacement of the hull and, consequently, reduced propeller thrust and propeller suction effect in this mode.

To conclude, significant unsteady loads on ESD were obtained in several series of measurements with ducts made of various materials in ballast and design conditions. Significant unsteady loads were also documented in CFD calculations. Even if the minimum values of these loads (data for the aluminium duct) are taken as estimates for the structural evaluation, the problems of fatigue strength at the points of attachment of the ducts to the hull of the vessel should be carefully taken into account.

7. Conclusions

Energy saving devices (ESD) have proved to be a promising way to improve ship efficiency and to reduce ship emissions and costs of operation. In the present paper, the bulker model $M1749S030$ with ship lines, which are close to the JBC benchmark test, equipped with the Mewis Energy Saving Duct was studied both experimentally and numerically. Since the steady hydrodynamic interaction between ship hulls, duct and propeller has already been studied in the past, the attention was paid primarily to unsteady effects caused by the wake non uniformity and wake turbulence, which are still not considered in the literature. To resolve the unsteady effect, the hybrid simulation

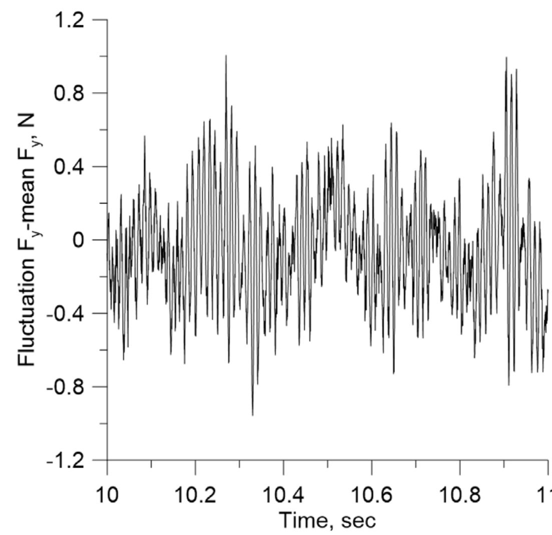

Fig. 10. Fluctuation of the force $F_y - \overline{F_y}$. EFD data obtained in design conditions for the aluminium duct.

based on the decomposition of the solution into LES (far from the hull surface) and RANS (close to the hull) regions was applied. For the sake of validation the bare hull resistance and the propeller diagram were calculated and compared with measurements of SVA Potsdam.

Both numerical and experimental investigations show that:

• The maximum turbulent pressure pulsations take place at points close to the leading edge of the duct. The biggest pressure pulsations are recorded in the corners at the junction of the duct and fin.

• The spectrum of pressure pulsations has a pronounced peak in a low frequency region both in CFD and EFD with and without propeller. Its presence is due to the interaction between the duct and the incoming vortex structures shed from the hull.

• The BPF pressure pulsation modes with propeller show a strong dominance of the first BPF mode, whereas the magnitudes of higher order modes are negligible and as a rule decrease with increase of BPF number.

• The agreement between CFD and EFD for unsteady pressure pulsations obtained above can be considered quite satisfactory, taking into account the moderate spatial and temporal resolutions used in CFD.

• The propeller suction increases the magnitude of pressure oscillations and, consequently, unsteadiness of forces on the duct.

• The fluctuation of all three force components on the duct is essential both in design and ballast conditions. This is the most important conclusion of this work from the practical point of view. The root mean squares of the fluctuation of axial, transverse and vertical forces are, respectively, 1.5, 0.8 and 0.4 percent of the total propeller thrust. Being multiplied with the cube of the scale factor λ for the real scale, these fluctuations point out on big amplitudes of unsteady forces which should be considered in structural analysis of ESD.

The revealed unsteady loads on the duct can be significantly enhanced during stopping and emergency reverse maneuvers as well as at heavy sea state conditions. These issues may become the subject of future works. Along with this, the scale effect on ESD remains a very acute problem in experimental ship hydromechanics.

CRediT authorship contribution statement

P. Anschau: Investigation, Validation, Data curation. **N. Kornev:** Investigation, Writing – original draft, Writing – review & editing. **S. Samarbakhsh:** Software, Investigation, Data curation.

Declaration of competing interest

The authors declare that they have no known competing financial interests or personal relationships that could have appeared to influence the work reported in this paper.

Data availability

Data will be made available on request.

Acknowledgments

The authors acknowledge gratefully the support of the German Federal Ministry for Economic Affairs and Energy (Bundesministerium für Wirtschaft und Energie) within the framework of the project HyDesign 03SX493D monitored by Dr. A. Nitz. The authors thank Steve Leonard (ibmv Maritime Innovationsgesellschaft mbH) for the STAR CCM+ computations using the IDDES SST model and Niklas Albertzard for the estimation of the turbulent flow around the duct.

References

Abbas, N., Kornev, N., 2016a. Study of unsteady loadings on the propeller under steady drift and yaw motion using URANS, hybrid (URANS-LES) and LES methods. Ship Technol. Res. 63, 121–131.

Abbas, N., Kornev, N., 2016b. Validation of hybrid URANS/LES methods for determination of forces and wake parameters of KVLCC2 tanker at maneuvering conditions. Ship Technol. Res. 63, 96–109.

Abbas, N., Kornev, N., Shvchuk, I., Anschau, P., 2015. CFD prediction of unsteady forces on marine propellers caused by the wake nonuniformity and nonstationarity. Ocean Eng. 104, 659–672.

Albertzard, N., 2022. Untersuchung der Instationaren Effekte an Mewis Duct mit OpenFOAM. Universität Rostock, Studienarbeit.

Bakica, A., Vladimir, N., Gatin, I., Jasak, H., 2020. CFD simulation of loadings on circular duct in calm water and waves. Ships Offshore Struct. http://dx.doi.org/10.1080/17445302.2020.1730082.

Celik, F., 2007. A numerical study for effectiveness of a wake equalizing duct. Ocean Eng. 34, 2138–2145.

Guiard, T., Leonard, S., Mewis, F., 2013. The becker mewis duct - challenges in full-scale design and new developments for fast ships. In: Proc. 3rd Int. Symp. Marine Propulsors SMP'13. Launceston, Tasmania, Australia.

Hollenbach, U., Reinholz, O., 2011. Hydrodynamic trends in optimizing propulsion. In: Proc. 2nd Int. Symp. Marine Propulsors SMP'11. Hamburg, Germany.

ITTC, 2014. Recommended procedures and guidelines: General guideline for uncertainty analysis in resistance tests.

Jasak, H., 1996. Error Analysis and Estimation for the Finite Volume Method with Applications to Fluid Flows (PhD thesis). Imperial College of Science, Technology and Medicine.

Juretić, F., 2022. Advanced meshing tool. https://cfmesh.com.

Kim, J., Choi, J., Choi, B., Chung, S., Seo, H., 2015. Development of energy-saving devices for a full slow-speed ship through improving propulsion performance. Int. J. Nav. Archit. Ocean Eng. 7, 390–398.

Korkut, E., 2006. A case study for the effect of a flow improvement device (a partial wake equalizing duct) on ship powering characteristics. Ocean Eng. 33, 205–208.

Kornev, N., Abbas, N., 2018. Vorticity structures and turbulence in the wake of full block ships. J. Mar. Sci. Technol. 23, 567–579.

Kornev, N., Shevchuk, I., Abbas, N., Anschau, P., Samarbakhsh, S., 2019. Potential and limitations of scale resolved simulations for ship hydromechanics applications. J. Ship Technol. Res. 66, 83–96.

Kornev, N., Taranov, A., Shchukin, E., Kleinsorge, L., 2011. Development of hybrid URANS-LES methods for flow simulation in the ship stern area. Ocean Eng. 38, 1831–1838.

Kume, K., Fukasawa, R., 2018. Experimental investigation of surface pressure distribution of the duct-type energy saving device for ships both in calm water and in wave conditions. In: 28th Int. Ocean and Polar Eng. Conf.. Sapporo, Japan.

Lee, I., Gose, J., Corradu, A., Chen, J., Hinatsu, M., Quereda, R., Li, T., 2021. The Specialist Committee on Energy Saving Methods. Final Report and Recommendations to the 29th ITTC.

Lungu, A., 2021. Energy-saving devices in ship propulsion: Effects of nozzles placed in front of propellers. J. Mar. Sci. Eng. 9, 1–24.

Menter, F., 1994. Two-equation eddy-viscosity turbulence models for engineering applications. AIAA J. 32 (8), 1598–1605.

Mewis, F., Guiard, T., 2011. Mewis duct- new developments, solutions and conclusions. In: Proc. 2nd Int. Symp. Marine Propulsors SMP'11. Hamburg, Germany.

Mewis, F., Hollenbach, U., 2006. Special measures for improving propulsive efficiency. In: HSVA NewsWave. The Newsletter from HSVA. Hamburg, Germany.

Mockett, C., Fuchs, M., Garbaruk, A., Shur, M., Spalart, P., Strelets, M., Thiele, F., Travin, A., 2015. Two non-zonal approaches to accelerate RANS to LES transition of free shear layers in DES. In: Progress in Hybrid RANS-LES Modelling. Springer, pp. 187–201.

Sakamoto, N., Kawanami, Y., Hinatsu, M., Uto, S., 2014. Viscous CFD analysis of stern duct installed on panamax bulk carrier in model and full scale. In: Proc. 13th Int. Conf. Computer and IT Applications in the Maritime Industries. Redworth, U.K..

Schuiling, B., 2013. The design and numerical demonstration of a new energy saving device. In: Proc. 6th Numerical Towing Tank Symposium (NuTTS). Müllheim, Germany.

Schuiling, B., Windt, J., Rijpkema, D., Terwisga, T., 2015. Computational study on power reduction by a pre-duct for a bulk carrier. In: Proc. Tokyo 2015, A Workshop on CFD in Ship Hydrodynamics, Vol. 3. Tokyo, Japan, pp. 331–336.

Shevchuk, I., Kornev, N., 2018. Improved version of LeMos hybrid model for ambiguous grid densities. Int. J. Nav. Archit. Ocean Eng. 10, 270–281.

Shin, H., Lee, J., Lee, K., Han, M., Hur, E., Shin, S., 2013. Numerical and experimental investigation of conventional and unconventional pre-swirl duct for VLCC. Int. J. Nav. Archit. Ocean Eng. 5, 414–430.

Shur, M., Spalart, P., Strelets, M., Travin, A., 2008. A hybrid RANS-LES approach with delayed-DES and wall- modelled LES capabilities. Int. J. Heat Fluid Flow 29, 1638–1649.

Taranov, A., 2021. private communication.

Terwisga, T., 2013. On the working principles of energy saving devices. In: Proc. 3rd Int. Symp. Marine Propulsors SMP'13. Launceston, Tasmania, Australia, pp. 510–518.

Weller, H.G., Tabor, G., Jasak, H., Fureby, C., 1998. A tensorial approach to computational continuum mechanics using object-oriented techniques. Comput. Phys. 12 (6), 620–631.

Yin, C., Wu, J., Wan, D., 2015. A numerical study for self-propelled JBC with and without energy saving device. In: Proc. Tokyo 2015, A Workshop on CFD in Ship Hydrodynamics, Vol. 3. Tokyo, Japan, pp. 395–400.